ChemCatChem

Research Article
doi.org/10.1002/cctc.202301704

Chemistry Europe
European Chemical Societies Publishing

www.chemcatchem.org

Non-Oxidative Conversion of Methanol to Dimethyl Ether, Methyl Formate and Dimethoxymethane over Cu/Hβ Catalyst: Tailoring Product Selectivity

Natalia Simitsis,[a] Chalachew Mebrahtu,*[a] and Regina Palkovits*[a, b]

Herein, we present the production of either dimethyl ether (DME), methyl formate (MF) or dimethoxymethane (DMM), representing pivotal molecules for the green transformation of fuels and chemical industry, by the non-oxidative gas-phase conversion of methanol under the same reaction conditions. The product selectivity is optimized by tailoring the acidic and dehydrogenative sites of the bifunctional Cu/Hβ catalyst system by varying the SiO_2/Al_2O_3 ratio of the Hβ zeolite (25 and 520) and the Cu loading (0.5 and 20 wt%). At 240 °C, >99% (DME), 74.5% (MF), and 77.3% (DMM) selectivity is achieved with the respective catalysts 0.5%Cu/Hβ(25), 20%Cu/Hβ(520), and 0.5% Cu/Hβ(520). High acidic site concentration catalyzes DME formation, while the presence of Cu^+ species is crucial for DMM formation, and Cu^0 species mainly catalyze MF formation. A highly dynamic reaction behaviour is observed, when the dehydrogenative functionality is dominant (*i.e.*, in the production of MF or DMM), presumably due to the dynamic nature of the Cu oxidation state, which is in turn influenced by possible by-products (H_2 and H_2O). While the catalytic activity in DME synthesis over 0.5%Cu/Hβ(25) is remarkably stable over 1500 min TOS, the activity in MF and DMM production over 20%Cu/Hβ(520) and 0.5%Cu/Hβ(520), respectively, can be successfully regenerated.

Introduction

In times of anthropogenic climate change and dwindling fossil fuels, the transition towards renewable feedstocks is inevitable. However, due to the fluctuating nature of renewable energy sources, such as wind and solar power, the conversion and storage of surplus energy from these renewable sources is crucial.[1] The conversion of CO_2 and green H_2 to produce methanol is considered as the pivotal reaction to transform fuels and chemical industry to renewable feedstocks referring to the "power-to-liquid" concept.[2] Methanol can be used as a fuel itself or be transformed into other high-performing fuels. Moreover, it is a base chemical used in the chemical industry for the synthesis of a plethora of further important chemicals, such as aldehydes, carboxylic acids, ethers etc.[3] When it comes to fuels, short oxygenated carbon-containing compounds, such as carbonates,[4] alcohols[5] and (poly)ethers,[6] have gained increased interest as clean diesel additives or substitutes.[7] Due to their high inherent oxygen content, significantly reduced soot formation during combustion eliminates the diesel-typical soot-NO_x trade-off. There is a high research interest in the production of these diesel additives and substitutes based on renewable feedstocks, such as methanol, which can be obtained from CO_2 and green H_2.[8,9]

Among possible oxygenated fuels derived from methanol, dimethyl ether (DME) is a highly interesting candidate. DME is a non-toxic gas under ambient conditions but is liquid above 5 bar and has many applications as fuel.[10] It has similar properties as liquefied petroleum gas (LPG) and can thus be used as a sustainable LPG blend, and also as gas turbine fuel in the power generation sector.[11] Due to its high cetane number of >55, which is even higher compared to diesel (>51) and its low auto-ignition properties,[10] it is a promising diesel substitute requiring only minor retrofitting of diesel engines.[12] Moreover, it serves as a sustainable feedstock for the production of olefins, from which polymers can be synthesized, substituting the conventional petrochemical-derived feedstocks.[13] Generally, DME synthesis occurs *via* methanol as an intermediate, either in a one-step process starting from CO or CO_2 and H_2 and direct conversion of methanol to DME in the same reactor, or in a two-step process with two separate reactors for methanol production and subsequent condensation to DME.[14,15] Both pathways are employed in industry and for the exothermic dehydration of methanol to DME, an acidic catalyst is needed.[16] The by-product water acts as an inhibitor for the dehydration of methanol since it interacts with the protons of the acidic catalyst and thus competes with methanol

[a] N. Simitsis, C. Mebrahtu, R. Palkovits
Institut für Technische und Makromolekulare Chemie (ITMC)
RWTH Aachen University
Worringerweg 2, Aachen 52074 (Germany)
E-mail: asmelash@itmc.rwth-aachen.de
palkovits@itmc.rwth-aachen.de
r.palkovits@fz-juelich.de

[b] R. Palkovits
Institut für nachhaltige Wasserstoffwirtschaft
Forschungszentrum Jülich GmbH
Brainergy-Park-Jülich, 52428 Jülich (Germany)

Supporting information for this article is available on the WWW under https://doi.org/10.1002/cctc.202301704

for the active site.[15,17,18] Many solid acid catalysts have been reported in methanol dehydration to DME, such as alumina,[19,20] mixed oxides,[21] zeolites[22] (H-ZSM,[23–25] CHA,[26] mordenite,[27] etc.), Al-SBA-15,[28] polymeric acids,[29] heteropoly acids[30] and more. However, the current challenge upon using the solid acid catalysts is to maintain high DME selectivity through suppressing the formation of hydrocarbons, and to prevent deactivation of the catalyst by water, DME, and coke.[18,23,31]

In addition to DME, methyl formate (MF) is a valuable base chemical derived from methanol. MF is an important building block in C_1 chemistry as it decomposes to CO and methanol and is thus a versatile process alternative to the toxic CO building block.[32] According to Bertau *et al.*, the overall increasing industrial implementation of green, methanol-based chemistry in the course of reducing CO_2 emissions requires a mastery of MF chemistry.[3] Other base chemicals that can be synthesized from MF include formic acid, dimethylformamide and other formamides, acetic acid, dimethyl carbonate, high purity CO as well as medical drugs.[33] Moreover, MF itself can be used as solvent, refrigerant (R611), blowing agent for polymers, binder in foundry processes and as a bactericide.[34] Similar to DME, it can also be used as oxygenated fuel and fuel additive.[35] MF has also attracted a lot of interest recently as green hydrogen carrier.[36] The major industrial production of MF is based on liquid-phase methanol carbonylation with CO, using a homogeneous sodium methoxide catalyst at 80 °C and 4.5 MPa.[3,37] Although 99% MF yield based on CO and methanol can be achieved, major drawbacks of this process include no catalyst recyclability, high raw material purity and a corrosion-resistant reactor (*i.e.*, due to the moisture sensitive, corrosive and homogeneous nature of the sodium methoxide catalyst), as well as the high operating pressure.[34] Another industrially applied MF synthesis pathway is methanol dehydrogenation with the formation of MF and H_2 as valuable by-product using a Cu-based catalyst (Mitsubishi Process).[38,39,40] However, as the reaction is endothermic, this pathway suffers from low methanol conversion due to the thermodynamic equilibrium limitations, which pose the major challenges of the dehydrogenative route. It is generally accepted that metallic Cu species are the active sites for methanol dehydrogenation.[39–43] Yang *et al.* performed mechanistic studies of methanol dehydrogenation to MF over Cu-based catalyst and they found that methanol is first dehydrogenated over Cu^0 sites to formaldehyde (FA).[41] MF is then formed by the reaction of FA with surface methoxy species over Cu^0 sites and not *via* the Tishchenko mechanism (*i.e.*, the dimerization of two FA molecules). They also found that Cu^+ species catalyze the decomposition of FA into CO and H_2. Hence, a catalyst with a dominant dehydrogenative functionality, such as metallic Cu species, is necessary for the selective dehydrogenation of methanol to MF. Other synthesis pathways for MF production are the oxidative dehydrogenation of methanol,[44] esterification of methanol and formic acid,[45] hydrogenation-condensation of CO_2 with methanol,[46] photocatalytic[47] and electrocatalytic[48] synthesis from methanol. Also very recently, the direct synthesis of MF from CO_2 and H_2 (and methanol), based on homogeneous Ru phosphine catalyst[49] as well as heterogeneous phosphine-polymer-anchored Ru catalyst[50] were reported.

In addition to DME and MF, dimethoxymethane (DMM), the shortest of the homologous oxymethylene ethers (OME_x) with the general structure of $H_3C\text{-}O\text{-}(CH_2\text{-}O)_x\text{-}CH_3$, as well as $OME_{3\text{-}5}$, have recently gained high research interest as clean diesel additives or substitutes as they eliminate the diesel-typical soot-NO_x trade-off.[7,51,52,53] While $OME_{3\text{-}5}$ are the more promising diesel substitutes due to their diesel-like physicochemical properties (viscosity, cetane number, vapor pressure, etc.),[52,54] DMM is more advantageous when used as a diesel additive because of its more energy-efficient production.[6,53,55,56] Besides, DMM is an important platform chemical to produce $OME_{3\text{-}5}$.[57] DMM is currently applied as solvent in chemical industry and serves as potential feedstock for concentrated FA production.[6] The established synthetic pathways for DMM rely on the oxidation of methanol with O_2 to FA and subsequent acetalization and condensation with two more methanol molecules.[6,9,58] Very recently, Bai *et al.* reported a metal-free N,O-codoped carbon catalyst for the oxidative dehydrogenation of methanol to DMM with high DMM selectivity of 75% at low reaction temperature (150 °C) and assigned the acidic and dehydrogenative active sites to carboxylic acid and carbonyl groups of the catalyst, respectively.[59] However, despite the good catalytic performances and technological readiness of the oxidative routes, the loss of valuable H_2 as H_2O causes low exergy efficiency and high carbon footprint, being the major disadvantage of the established routes.[53,55,60] Besides CO_2 reduction with H_2 to form DMM, which was recently published by Klankermayer and co-workers,[61] the continuous gas-phase non-oxidative dehydrogenation (NOD) of methanol to DMM, with the formation of H_2 instead of H_2O, is a captivating route for technical implementation.[6] Here, methanol is first dehydrogenated without the presence of an oxidizing agent to FA and H_2 in an endothermic reaction. The subsequent exothermic acetalization and condensation with methanol to DMM shift the reaction equilibrium towards the product site.[62] Hence, for the one-step NOD of methanol to DMM, a bifunctional catalyst with both dehydrogenative and acidic functionality is required. Here, the first catalyzes the methanol dehydrogenation to the intermediate FA, releasing H_2, while the latter catalyzes the acetalization of FA with methanol to form an intermediate hemiacetal, which then condenses (also acid-catalyzed) with another methanol molecule to form DMM.[6] However, both functionalities individually catalyze the formation of DME and MF, respectively. Only few catalyst systems for the NOD of methanol to DMM in the gas-phase have been reported so far.[62–65] Our group recently designed a highly selective, bifunctional catalyst with dispersed Cu nanoparticles supported on Si-rich Hβ zeolite.[62] In this study, different zeolites (*i.e.*, Hβ (BEA topology), HY (FAU topology), and HZSM-5 (MFI topology)) were screened as catalyst supports, showing that the product distribution highly depends on the acidic strength and acidic site concentration of the respective zeolite support. Of the tested zeolites, Hβ shows the highest DMM selectivity compared to the other zeolites. Based on that, in our next study, Hβ zeolite was dealuminated in order to tailor its acidic sites.[63] Together with a low Cu

loading of 1 wt% (catalyzing the methanol dehydrogenation to FA), an optimal SiO_2/Al_2O_3 ratio of 520 was found to be beneficial for high DMM selectivity, mainly allowing acetalization of FA with methanol. With the optimized bifunctional Cu/Hβ catalyst, DMM selectivity increases to 81.5% with a methanol conversion of 3.7% at 200 °C in 1500 min time on stream (TOS), for which the evolution of both Lewis acidic sites and an optimal ratio of Cu^+/Cu^0 sites are responsible. However, the long induction time of 800 min, low catalyst stability (*i.e.*, a decrease in methanol conversion from 5.6% to 3.7% after 1500 min TOS), and low conversion when compared to the calculated equilibrium conversion (7.6%) are the existing challenges upon using the Cu/Hβ bifunctional catalyst.

As discussed above, the design of a highly active, selective and stable catalyst remained a challenge for the synthesis of DME, MF and DMM. Hence, herein, we present the production of DME, MF and DMM under the same reaction conditions by the non-oxidative gas-phase conversion of methanol over a versatile Cu/Hβ catalyst with tailored acidic sites and dehydrogenative properties (Scheme 1). For this, the Cu loading (0.5 and 20 wt%) and the SiO_2/Al_2O_3 ratio of the Hβ zeolite (25 and 520) are tailored and the selectivity towards DME, MF and DMM is investigated under similar reaction conditions. Catalyst stability tests under extended time on stream are performed and successful regeneration strategies are employed for the deactivated catalysts. Moreover, possible structure-activity relationships are proposed based on the catalyst characterization results obtained from XRD, N_2-physisorption, ICP-OES, H_2-TPR, CO-DRIFTS, and pyridine adsorption FTIR (py-FTIR). The goal of this work is therefore to gain deeper understanding on this complex reaction network and shed light on tailoring active sites for the formation of the different products over the Cu/Hβ catalyst.

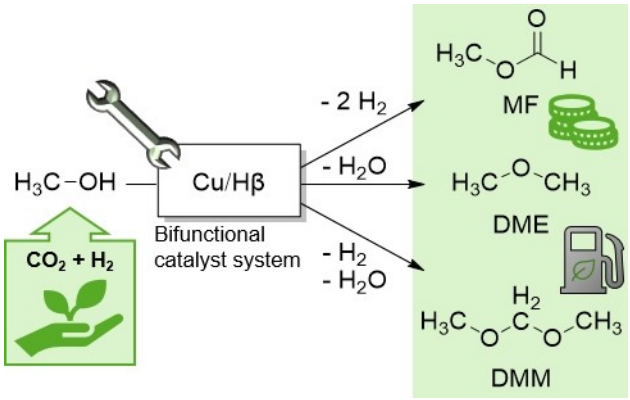

Scheme 1. Overview of the gas-phase, non-oxidative methanol conversion to the valuable products methyl formate (MF), dimethyl ether (DME), and dimethoxymethane (DMM), which can be obtained under similar reaction conditions by engineering the bifunctional Cu/Hβ catalyst system.

Results and Discussion

Catalyst Characterization

In our previous work, a correlation between the SiO_2/Al_2O_3 ratio of the Hβ zeolite support, the Cu loading and the corresponding product selectivity in the non-oxidative methanol conversion was observed.[63] Based on the trends observed in this previous study, optimized SiO_2/Al_2O_3 ratios and Cu loadings were chosen for the bifunctional Cu/Hβ catalyst in the current study in order to tailor the catalytic properties and the product selectivity. Hence, in this study, Hβ(25) was used (obtained from commercial NH_4β by calcination) and dealuminated by acid treatment to increase the SiO_2/Al_2O_3 ratio to 520, according to our previous report.[63] The parent Hβ(25) was loaded with 0.5 wt% Cu by incipient wetness impregnation (IWI), and the dealuminated Hβ(520) was loaded with both 0.5 and 20 wt% Cu. The materials are denoted as *X*%Cu/Hβ(*Y*), where *X* and *Y* remark the Cu loading in wt% and the SiO_2/Al_2O_3 ratio of the zeolite, respectively.

Physicochemical properties of the Cu loaded zeolite samples were first investigated by ICP-OES and N_2-physisorption and the obtained results are given in Table 1. The measured Cu loadings by ICP-OES are close to the respective nominal loadings used during the synthesis. The N_2-physisorption isotherms (Figure S1, SI) show a plateau at low partial pressures which is typical for microporous materials (type I isotherm) with a narrow hysteresis loop at higher partial pressures which presumably arises from mesoporous cavities between the zeolite particles.[66] Besides, the surface areas (S_{BET}) of 0.5 wt% Cu loaded on either Hβ(25) or Hβ(520) sample do not significantly differ (*i.e.*, 544 and 555 m^2/g, respectively). But, the dealumination leads to an increased mesopore volume of 0.62 mL/g for 0.5%Cu/Hβ(520) compared to 0.53 mL/g of 0.5%Cu/Hβ(25), which is in line with Baranowski *et al.*[67] When 20 wt% Cu are loaded on Hβ(520), the S_{BET} decreases to 430 m^2/g which is accompanied by a significant decrease in both micro- and mesopore volumes (*i.e.*, 0.13 and 0.46 mL/g, respectively). Hence, due to the high Cu loading, the pores of the zeolite are presumably partially blocked, resulting

Table 1. Elemental composition and textural properties of the Cu/Hβ samples. The Cu loading is based on ICP-OES analysis. Based on N_2-physisorption, the surface area (S_{BET}) is calculated by the BET method, and the micro-pore volume by the t-plot method. The acidic sites are quantified by means of pyridine adsorption FTIR (py-FTIR).

Sample	Cu loading (wt%)	S_{BET} (m^2/g)	Volume (mL/g)			Acidic sites (μmol/g)		
			Total	Micro-pore	Meso-pore	Brønsted sites	Lewis sites	Total acidic sites
0.5%Cu/Hβ(25)	0.44	544	0.69	0.16	0.53	115	67	182
0.5%Cu/Hβ(520)	0.54	555	0.76	0.14	0.62	n.d.	4	4
20%Cu/Hβ(520)	19.8	430	0.59	0.13	0.46	n.d.	33	33

in decreased accessible S_{BET} and pore volume of the 20%Cu/Hβ(520) catalyst.

The XRD patterns of Hβ(25) and Hβ(520) as well as the Cu loaded Hβ samples are depicted in Figure S2, SI. No significant structural change of Beta zeolite can be observed due to dealumination, as was already discussed in our previous work.[63] However, a slightly decreased intensity of the diffraction signals after Cu introduction and calcination of Hβ(520) can be observed in this work, indicating a less crystalline structure of Cu loaded Hβ(520). Yet, the intensity of the diffraction signals might also be affected by a different amount of sample used for the XRD measurements. In Figure 1-I, diffraction patterns are shown for the calcined Cu loaded Hβ samples together with a diffractogram of CuO which was simulated by VESTA based on the CuO space group.[68] The samples with a low Cu loading of 0.5 wt% do not show any diffraction signals of Cu oxide species, indicating either high dispersion of the Cu species or that the Cu loading is below the detection limit. In contrast, high Cu loading of 20 wt% results in intense diffraction signals of CuO species, indicating the formation of large CuO particles on the 20%Cu/Hβ(520) sample.[69,70] To investigate reducibility of the Cu loaded Hβ zeolite samples, H_2-TPR measurements were performed (Figure 1-III). The 20%Cu/Hβ(520) sample shows one single reduction peak at 331 °C, which is typical for bulk CuO with an instantaneous reduction of $Cu^{2+} \rightarrow Cu^0$,[71] being in line with the XRD results. Decreasing the Cu loading on the dealuminated Hβ(520) to 0.5 wt% leads to the formation of two well separated reduction peaks at 277 °C and 444 °C, respectively. These reduction signals are known in literature as the two consecutive reduction steps of Cu^{2+} to Cu^+ (< 350 °C) and Cu^+ to Cu^0 (> 350 °C), which is typical for highly dispersed CuO species[71,72] and were also observed in our previous report for 1%Cu/Hβ(520).[63] The same 0.5 wt% Cu loading on the parent Hβ(25) zeolite results in a broad, overlapped signal with two peaks at 271 °C and 331 °C, respectively. This indicates a broad distribution of the reduction of various CuO species, arising from inhomogeneous dispersion and varying metal-support interaction. In our previous work, similar results were observed for 1%Cu/Hβ(25).[63] It is generally known in literature that the closer two Cu^{2+} ions are present on a support, the smaller the temperature difference of the two-reduction steps get.[70] Hence, it can be concluded that the calcined 0.5%Cu/Hβ(520) possesses highly dispersed Cu^{2+} species compared to the other Cu/Hβ samples. In order to investigate the metal-support interaction of the Cu/Hβ samples, H_2-TPR of a physical mixture of CuO and Hβ(520) with 20 wt% Cu was also used, showing a broad reduction signal with a maximum at 325 °C. In comparison to that, all Cu/Hβ samples prepared by impregnation show reduction signals at higher temperatures, indicating a stronger metal-support interaction due to the employed impregnation method compared to simple physical mixing of CuO and Hβ zeolite. Generally, based on the H_2-TPR results obtained, all the Cu/Hβ samples show significantly different reduction properties depending both on the Cu loading as well as on the SiO_2/Al_2O_3 ratio of the Hβ zeolite. And, this will lead to the formation of different Cu species (Cu^{2+}, Cu^+ and Cu^0) during the *in situ* reduction and reaction. Since the obtained H_2-TPR results of 20%Cu/Hβ(520) and 0.5%Cu/Hβ(520) show a significant difference, and it is known that the ratio of Cu^+/Cu^0 species formed after reduction plays a crucial role for the product distribution and activity in the NOD of methanol,[41,63] CO-DRIFTS measurements were performed in order to investigate the Cu oxidation state. CO-DRIFTS is a common technique to observe whether Cu^+ species are present on Cu/zeolite materials because CO

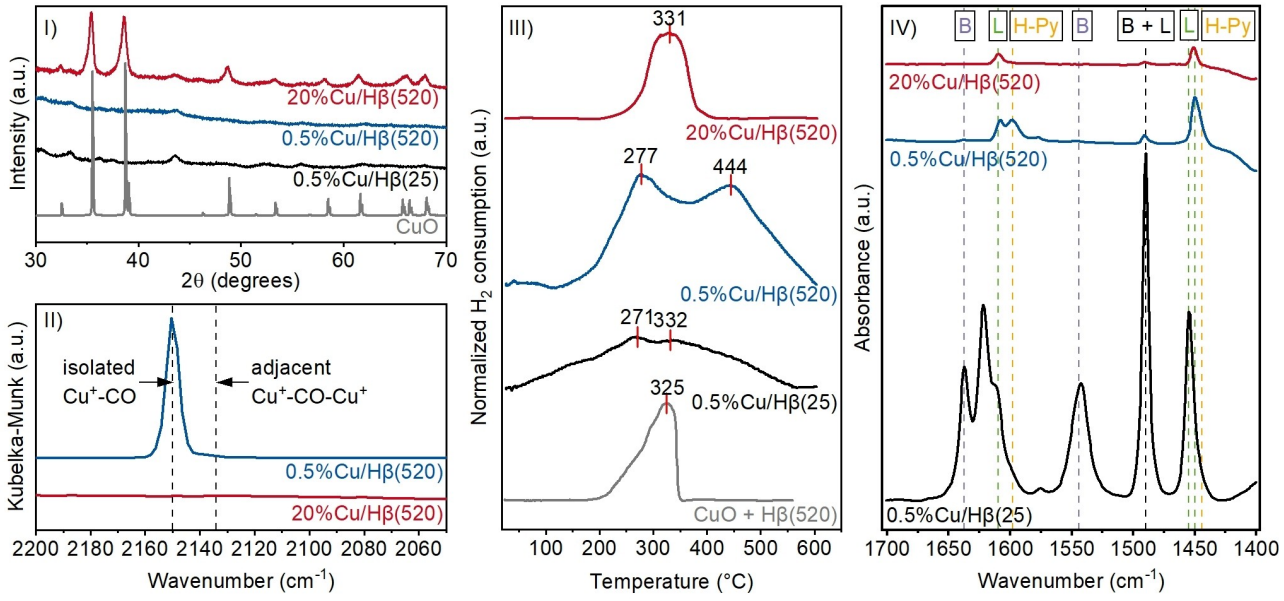

Figure 1. I) Powder XRD patterns of the calcined Cu/Hβ samples and the powder XRD pattern of CuO, which was simulated with VESTA based on the space group of CuO;[68] II) CO-DRIFTS of Cu/Hβ(520) samples after *in situ* reduction treatment (450 °C, 3 h, 20 °C/min); III) H_2-TPR results for the calcined Cu loaded Hβ samples and a physical mixture of calcined CuO and calcined Hβ(520) with 20 wt% Cu. The H_2 consumption was normalized to the amount of Cu and a baseline correction was performed.; IV) Pyridine adsorption FTIR (py-FTIR) results of the calcined Cu/Hβ samples.

adsorbs strongly on Cu^+ at room temperature, while it is easily desorbed from Cu^0 during flushing and hardly adsorbs on Cu^{2+}.[73] Hence, in order to understand which Cu species are present initially after the *in situ* reduction (at the start of the reaction), 20%Cu/Hβ(520) and 0.5%Cu/Hβ(520) were reduced *in situ* (in the DRIFTS cell), then cooled to 30 °C under N_2, and then CO adsorption was performed until saturation. After the desorption of CO under N_2 flow, it can be seen from Figure 1-II that 0.5%Cu/Hβ(520) exhibits an intense signal at 2150 cm^{-1}, which is typical for CO adsorbed on isolated Cu^+ species,[74,75] indicating isolated Cu^+ species being initially present at the start of the reaction (*i.e.*, after the *in situ* reduction). Moreover, a small shoulder at 2134 cm^{-1} can be observed for this sample, which typically represents the vibration of CO adsorbed on two adjacent Cu^+, indicating close proximity of those Cu^+ species.[70,74,76] However, since this signal is very weak, the main Cu^+ species initially present after reduction are isolated Cu^+ species. In contrast, 20%Cu/Hβ(520) does not show any CO adsorption after the *in situ* reduction, indicating the presence of only Cu^0 on the surface of possible Cu particles (since the presence of Cu^{2+} can be excluded due to the reduction treatment). These results are in line with H_2-TPR results which show facilitated reduction of 20%Cu/Hβ(520) at lower reduction temperatures compared to 0.5%Cu/Hβ(520) that rather possesses isolated Cu species which are harder to reduce compared to bulk CuO. This could be attributed to the stronger metal-support interaction formed over the 0.5%Cu/Hβ(520) compared to 20%Cu/Hβ(520).

Furthermore, py-FTIR of the calcined Cu/Hβ samples was measured to identify the type and concentration of acidic sites and the obtained spectra are depicted in Figure 1-IV. Pyridine adsorption over the 0.5%Cu/Hβ(25) sample results in vibration bands at 1544 cm^{-1} and 1636 cm^{-1} corresponding to the adsorption on Brønsted acidic sites, and at 1610 cm^{-1} and 1454 cm^{-1} corresponding to the adsorption on Lewis acidic sites. Besides, the shoulders at 1597 cm^{-1} and 1444 cm^{-1} correspond to hydrogen-bonded pyridine on silanol groups of the zeolite. The band at 1490 cm^{-1} corresponds to the overlapping adsorption of pyridine on Brønsted and Lewis acidic sites.[77] Accordingly, the Cu/Hβ(520) samples show a shift of the pyridine vibration bound to a Lewis acidic site to 1450 cm^{-1} and no vibrations corresponding to Brønsted acidic sites are observed. The quantification of Brønsted acidic sites is based on the integration of the band at 1544 cm^{-1} (which is only present for 0.5%Cu/Hβ(25)). The bands at 1454 cm^{-1} and 1450 cm^{-1} for Cu loaded Hβ(25) and Hβ(520), respectively, with the shoulder at 1444 cm^{-1}, were deconvoluted into two components and the respective bands at 1454 cm^{-1} and 1450 cm^{-1} were integrated for Lewis acidic site quantification (see Figure S3, SI, as an example for the deconvolution method employed). Table 1 summarizes the quantified amount of Brønsted and Lewis acidic sites of the Cu/Hβ samples. The total amount of acidic sites (both Brønsted and Lewis type), is highest for 0.5%Cu/Hβ(25) with a total acidic site concentration of 182 μmol/g. This is expected due to its low SiO_2/Al_2O_3 ratio compared to Hβ(520), as it is generally known that the amount of Al in the zeolite framework corresponds with the amount of acidic sites.[78] Thus, dealumination and subsequent Cu impregnation and calcination leads to a significant reduction of both Brønsted and Lewis acidic sites, as has been previously reported.[63] The removal of all detectable Brønsted acidic sites for the Cu loaded Hβ(520) can be attributed to the dihydroxylation of any remaining framework Al during the calcination process after Cu impregnation, forming extra-framework Al species possessing Lewis acidity.[79] Moreover, increased Cu loading on Hβ(520) of 20 wt% increases the Lewis acidic site concentration compared to 0.5 wt% Cu loading (33 vs. 4 μmol/g, respectively). This might originate from the increased amount of weakly Lewis acidic Cu^{2+} species due to the high Cu loading.[80] Thus, the acidity of the bifunctional Cu/Hβ catalyst does not only depend on the SiO_2/Al_2O_3 ratio of the Hβ zeolite, but also on the Cu loading and possible Cu species formed. Our previous study also shows that the concentration of Lewis acidic sites on 1% Cu/Hβ(520) strongly depends on the catalyst treatment, such as reduction or reaction, (besides the SiO_2/Al_2O_3 of the Hβ zeolite).[63] This suggests that also the Cu oxidation state has an influence on the Lewis acidic sites and thus the acidic and dehydrogenative sites of the bifunctional Cu/Hβ catalyst system might be interdependent. All in all, based on the py-FTIR measurements, it can be concluded that 0.5%Cu/Hβ(25) exhibits by far the highest concentration of both Lewis and Brønsted acidic sites, followed by a medium Lewis acidic site concentration for 20%Cu/Hβ(520) and very low Lewis acidic site concentration for 0.5%Cu/Hβ(520).

Catalytic Tests

The prepared Cu/Hβ materials were tested in the gas-phase, non-oxidative conversion of methanol under the same reaction conditions (240 °C, 1 atm, 14549 mL/h*g_{cat}) in order to investigate the product selectivity depending on the dehydrogenative and acidic properties of the catalysts. Figure 2 shows the catalytic results for 0.5%Cu/Hβ(25), 0.5%Cu/Hβ(520), and 20% Cu/Hβ(520) after 1500 min TOS. Low Cu loading and low SiO_2/Al_2O_3 ratio of the 0.5%Cu/Hβ(25) sample result in almost exclusive formation of DME (>99% selectivity with the formation of trace amounts of CH_4 and short C_2-C_4 hydrocarbons, Figure S5, and Table S1, SI) with a high methanol conversion of 82.2%. Besides, no decrease in catalytic activity (catalyst deactivation) could be observed during the 1500 min TOS (Figure S4, SI). When Hβ(25) is used without Cu, DME remains the main product with >99% selectivity and a slightly lower methanol conversion of 80.9% with the formation of trace amounts of CH_4 and short C_2-C_4 hydrocarbons (Figure S6 and S7, SI). The remarkable activity, DME selectivity and stability of 0.5%Cu/Hβ(25) make this catalyst system even superior compared to the industrially used alumina-based catalysts[20,81,82] and comparable to other zeolite-based catalysts.[16,24,83] When the SiO_2/Al_2O_3 ratio is increased to 520 by dealumination, DMM becomes the main product with a selectivity of 77.3% and a methanol conversion of 2.2% after 1500 min TOS. When the Cu loading is increased further to 20 wt% on the dealuminated Hβ(520), the main product is switched to MF with a selectivity

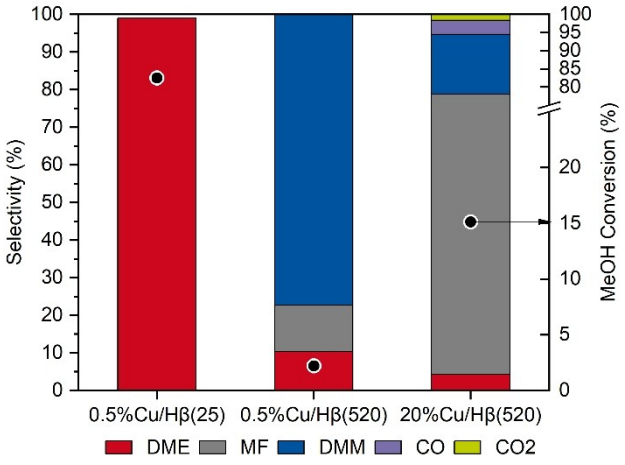

Figure 2. Screening of Cu/Hβ catalysts with varying SiO_2/Al_2O_3 ratio and Cu loading in the gas-phase, non-oxidative conversion of methanol. Reaction conditions: 240 °C, 1 atm, GHSV = 14549 mL/h*g_{cat}, 0.1 g of catalyst diluted with 0.9 g of SiC, n(CH_3OH)/n(N_2) = 0.24, N_2 flow rate = 19.4 mL/min, *in situ* reduction prior to reaction (450 °C, H_2-flow = 20 mL/min, 3 h). Results shown after 1500 min TOS.

of 74.5% and a methanol conversion of 15.1%. Since CO is known to be the major side product in MF formation from methanol dehydrogenation,[43] CO and CO_2 were quantified by an offline GC equipped with a TCD when using 20%Cu/Hβ(520) as catalyst. However, for both CO_2 and CO, only low amounts (*i.e.*, below 5% selectivity) are observed. In order to evaluate the product formation in terms of the thermodynamic equilibrium, the yields of DMM and MF are considered and compared to the thermodynamic equilibrium yield under the assumption of a 100% selective catalyst (Figure S8, SI for thermodynamic equilibrium). Thus, the yield of DMM and MF of 1.7% and 11.2% correspond with 20.0% and 31.3% of the thermodynamic equilibrium yield at 240 °C, respectively.[62] Furthermore, to check whether the product distribution of MF and DMM is affected by the methanol conversion, 20%Cu/Hβ(520) was tested at a higher GHSV of 72572 mL/h*g_{cat} (Figure S9, SI). After 1500 min TOS, at a methanol conversion of 1.7%, MF remains the main product with a selectivity of 79.2%, while the selectivity towards DMM is 20.0%.

Besides, both Cu/Hβ(520) samples show deactivation during 1500 min TOS (*i.e.*, methanol conversion loss of 33% and 67% for 0.5%Cu/Hβ(520) and 20%Cu/Hβ(520), respectively), and induction times over 1500 min, indicating a highly dynamic reaction course (Figure 3 a and b). The deactivation of Cu based catalysts is often linked to carbon deposition on the catalyst,[84] Cu particle sintering or changes of the Cu oxidation state during the reaction.[76,85] However, since no organic residues were observed on the spent Cu/Hβ catalyst in our previous studies based on TG-MS and ATR-IR,[62] and the formation of hydrocarbons ($C_{\geq 2}$) is not detected over 0.5%Cu/Hβ(520) and 20% Cu/Hβ(520), carbon deposition can be excluded as a reason for the catalyst deactivation. Hence, if the deactivation is mainly caused due to a change in Cu oxidation state during the reaction, the spent catalyst can be re-calcined and re-reduced to regenerate the catalytic activity by restoring the initial Cu oxidation state. Thus, after 1500 min TOS, the methanol feed was stopped, the reactor was cooled to room temperature under N_2 flow and the catalyst was subsequently re-calcined and re-reduced *in situ*. Figure 3 a) and b) show that for both 0.5%Cu/Hβ(520) and 20%Cu/Hβ(520), the overall catalytic performance could be fully restored after the regeneration. Similar catalytic performance as in the first run over a fresh catalyst is obtained, suggesting the crucial role of the Cu oxidation state for both product selectivity and methanol conversion. Interestingly, both the MF and DME selectivity decrease during the reaction course and then increase to the initial values of the first run after the regeneration treatments. This suggests that the Cu oxidation state affects both the acidic and dehydrogenative functionality of the bifunctional Cu/Hβ

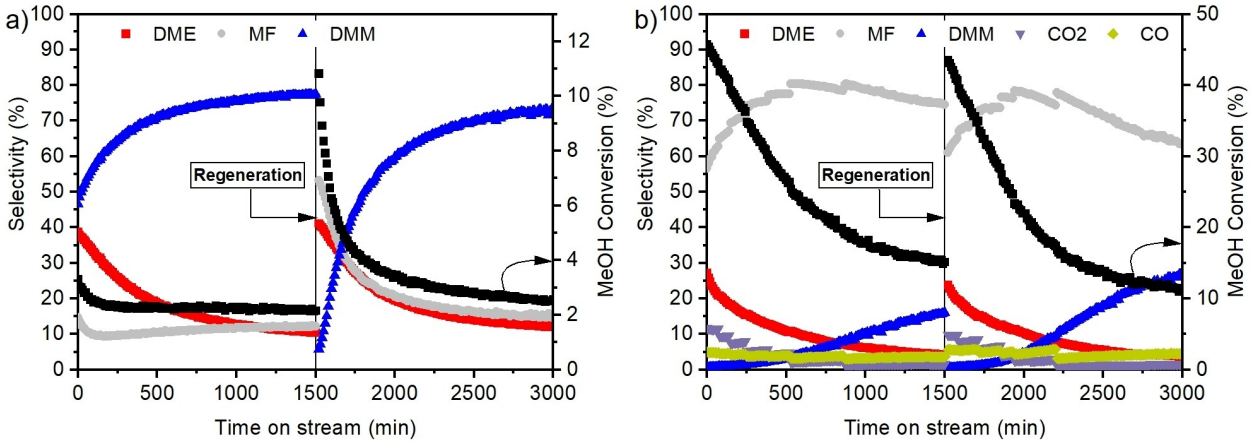

Figure 3. Catalytic results for the gas-phase, non-oxidative conversion of methanol over a) 0.5%Cu/Hβ(520) and b) 20%Cu/Hβ(520) including regeneration by re-calcination and re-reduction after 1500 min TOS. Reaction conditions: 240 °C, 1 atm, GHSV = 14549 mL/h*g_{cat}, 0.1 g of catalyst diluted with 0.9 g of SiC, n(CH_3OH)/n(N_2) = 0.24, N_2 flow rate = 19.4 mL/min, *in situ* reduction prior to reaction (450 °C, H_2-flow = 20 mL/min, 3 h). Regeneration was performed by first cooling the reactor down to room temperature under N_2 flow after 1500 min TOS, which was followed by *in situ* re-calcination (450 °C, syn. air flow = 20 mL/min, 3.5 h) and re-reduction (450 °C, H_2-flow = 20 mL/min, 3 h).

catalyst, which is in line with the dynamic changes of the Lewis acidic site concentration depending on both the Cu loading (Table 1) and the catalyst treatment and thus possibly the Cu oxidation state as shown in our previous report.[63] Therefore, combined with the characterization results, the catalyst regeneration experiments provide evidence into the role of the Cu oxidation state and enable to draw possible structure-activity relationships using the Cu oxidation state as a descriptor.

Potential of the Cu/Hβ Catalyst System

The performance of the Cu/Hβ catalyst system employed in this work for the selective synthesis of DME, MF, and DMM is compared to literature data. Table 2 lists the catalytic results (*i.e.*, selectivity (S), methanol conversion (X), stability of the catalyst) as well as the reaction parameters employed in this work and recent publications. Full DME selectivity, high methanol conversion of >80% and high stability during 1500 min TOS over 0.5%Cu/Hβ(25) make this catalyst superior to reported Al_2O_3-based catalysts[20,82] and comparable to other zeolite-based materials.[83] In contrast, MF production over 20% Cu/Hβ(520) catalyst is less selective and the catalyst is less active compared to other Cu-based catalysts reported in literature, but Wang *et al.*[86] and Jin *et al.*[87] used harsher reaction conditions (*i.e.*, higher temperature, and/or pressure). Moreover, although the core-shell 7%Cu/SiO_2 catalyst shows superior selectivity and activity in the methanol dehydrogenation to MF compared to the 20%Cu/Hβ(520) catalyst at similar reaction conditions, the catalyst synthesis procedure of 20%Cu/Hβ(520) employed in this work is faster and does not employ organic substances compared to the Stöber synthesis employed for the core-shell 7%Cu/SiO_2 catalyst.[41] Next, DMM production over 0.5%Cu/Hβ(520) results in the highest DMM selectivity when compared to other published Cu-based catalysts at similar reaction conditions.[63–65] Although the methanol conversion of 0.5%Cu/Hβ(520) is comparably low, the successful regeneration and the overall lowest reported metal loading make the 0.5%Cu/Hβ(520) catalyst highly attractive compared to other reported Cu-based catalysts for DMM production *via* the NOD of methanol.

Structure-Activity Relationship

A possible structure-activity relationship of the tailored Cu/Hβ catalysts is supposed based on the results of the catalytic tests in combination with XRD, H_2-TPR, CO-DRIFTS, and py-FTIR results. High acidic site concentration of both Brønsted and Lewis acidic sites as detected by py-FTIR seems to be responsible for the exclusive formation of DME over 0.5%Cu/Hβ(25) (Table 1 and Figure 1-IV). As depicted in Figure 2, removing all detectable Brønsted acidic sites and significantly decreasing the Lewis acidic site concentration after dealumination of Hβ(25) leads to significantly decreased DME selectivity of 10.4% over 0.5%Cu/Hβ(520) and 4.2% over 20%Cu/Hβ(520) after 1500 min TOS as well as a switch of the main product to either DMM or MF. Hence, the limited acidic sites present on

Table 2. Potential of the Cu/Hβ catalyst system compared to recent reported catalysts for the synthesis of DME, MF, or DMM, respectively, from methanol. Hereby, S denotes the selectivity towards the respective main product and X denotes the methanol conversion.

Product	Catalyst	S	X	Stability	Reaction parameters	Ref.
DME	0.5%Cu/Hβ(25)	>99%	82.2%	Stable during 1500 min TOS	240 °C, 1 atm, GHSV = 14549 mL/h*g_{cat} (WHSV = 3.8 g_{MeOH}/h*g_{cat})	this work
MF	20%Cu/Hβ(520)	74.5%	15.1%	Regeneration possible		
DMM	0.5%Cu/Hβ(520)	77.3%	2.2%	Regeneration possible		
DME	γ-Al_2O_3	>99%	~80%	Deactivation	250 °C, 1 atm, WHSV = 3 h^{-1}	[20]
DME	CuO-Fe_2O_3/Al_2O_3	100%	70%	Deactivation	290 °C, 1 atm, WHSV = 1.3 h^{-1}	[82]
DME	Nano-sized FER zeolite	99%	84%	Stable during 1200 min TOS	240 °C, 1 atm, WHSV = 4 g/h*g_{cat}	[83]
MF	Core-shell 7%Cu/SiO_2	83.8%	39.1%	Regeneration possible	230 °C, 1 atm, WHSV = 4 h^{-1}	[41]
MF	20%Cu–Zn/SBA-15	88.1%	31.1%	Slight deactivation during 6000 min TOS	300 °C, 20 bar, $LHSV_{MeOH}$ = 7.9 h^{-1}	[86]
MF	20%Cu/ZSM-5 (Si/Al = 50)	88.3%	35.0%	Stable during 600 min TOS	300 °C, 1 atm, GHSV = 12047 mL/h*g_{cat}	[87][a]
DMM	3%Cu/ZrAl oxide	12.0	24.7%	Stable during 1320 min TOS	200 °C, 1.7 atm, WHSV = 1.3 h^{-1}	[64]
DMM	1%Cu/Hβ(520)	59.7%	6.8%	Deactivation	240 °C, 1 atm, GHSV = 14549 mL/h*g_{cat}	[63]
DMM	3%Cu/sulfated-ZrO_2	63.6%	6.4%	Stable during 720 min TOS (200 °C)	250 °C, 1 atm, GHSV = 9628 mL/h*g_{cat}	[65][a]

[a] Values for GHSV shown here were calculated from data given in the references.

the Cu loaded Hβ(520) catalysts do not dominate the reaction outcome which in turn leads to low DME selectivity. Previous studies claim that the formation of an appropriate Cu^+/Cu^0 ratio might be responsible for high DMM selectivity, and its evolution during the reaction course causes long induction times for DMM production.[62,63] Moreover, Cu^0 is supposed to be the active site for methanol dehydrogenation to MF,[39,86,87] while Cu^+ leads to FA decomposition into CO and H_2.[41] Therefore, under these conditions, it can be assumed that the product distribution over Cu/Hβ(520) catalysts is mainly controlled by the Cu oxidation state formed, playing a key role in shaping the product selectivity in the non-oxidative methanol conversion. It needs to be added that, even though the Lewis acidic sites concentration increases with increased Cu loading (*i.e.*, from 4 to 33 μmol/g for 0.5 and 20 wt% Cu, respectively, Table 1), the dehydrogenative functionality still outweighs the acidic functionality of 20%Cu/Hβ(520) as can be observed from the high MF selectivity compared to the DME selectivity in the catalytic test (Figure 2 and Figure 3b). The dehydrogenative functionality can thus be regarded as the dominant functionality on the 20% Cu/Hβ(520) catalyst. Thus, based on XRD, CO-DRIFTS, and H_2-TPR results (Figure 1-I, -II, and -III), the possible dynamic changes of the Cu oxidation state of 0.5%Cu/Hβ(520) and 20% Cu/Hβ(520) during the reaction and regeneration are combined with the respective product selectivity and schematically represented in Figure 4. Considering 0.5%Cu/Hβ(520), CO-DRIFTS and H_2-TPR results suggest the presence of highly dispersed Cu^+ species at the start of the reaction. However, the presence of Cu^0 on the initial catalyst after the reduction cannot be excluded as higher *in situ* reduction temperature was used (450 °C). This is also in line with Kefirov *et al.* who investigated ion-exchanged Cu-BEA and observed mainly Cu^+ with some Cu^0 species after reduction at 450 °C based on CO-DRIFTS and H_2-TPR analysis.[88] A long induction time of >1500 min TOS with an increase in DMM selectivity is then observed in the reaction (Figure 3 a), presumably due to the evolution of an appropriate ratio of Cu^+/Cu^0 species.[63,89] After the regeneration, 0.5%Cu/Hβ(520) regains very high activity with an initial methanol conversion of 10.8% and MF being the main product with a selectivity of 53.2%, while the selectivity towards DMM is decreased to 5.7%. This might be explained by the possibly high amount of Cu^0 on the initial catalyst after the regeneration due to the double reduction. However, after 200 min TOS, DMM selectivity surpasses MF selectivity and further increases to 73.1% after 1500 min TOS, presumably due to the renewed formation of the appropriate ratio of Cu^+/Cu^0 species resulting from the re-oxidation of some of the Cu^0 species to Cu^+. Since both H_2 and H_2O are the by-products of DMM formation from methanol dehydrogenation, their reducing or oxidizing potential might be the reason for the dynamics of the Cu oxidation state during the catalytic tests.

In contrast, when the Cu loading is increased to 20 wt%, bulk Cu^0 is suggested to be present on the initial catalyst after *in situ* reduction (based on XRD, CO-DRIFTS and H_2-TPR results), which is known to mainly catalyzing the formation of MF.[39,41,86,87] To check whether bulk Cu^0 is sufficient for MF production or if metal-support interaction plays a role for the formation of MF, a physical mixture of CuO and Hβ(520) with 20 wt% Cu was tested as catalyst under the same pre-treatment and reaction conditions (see Figure S10, SI). However, Cu species in this mixture seem to be inactive since the catalytic results do not differ significantly from Hβ(520) without CuO (*i.e.*, high DME formation of ~80%, low methanol conversion of 0.7% after 1500 min TOS, see Figure S11, SI). Hence, the metal-support interaction between Cu species and Hβ(520), arising from the impregnation and calcination procedure when compared to the physical mixture of CuO and Hβ(520), which is also observed in H_2-TPR by the shift towards higher reduction temperatures (Figure 1-III), is necessary for the dehydrogenative activity in methanol conversion. Considering the reaction course over 20%Cu/Hβ(520) catalyst (Figure 3 b), an initial increase in MF selectivity up to 80.4% can be observed until

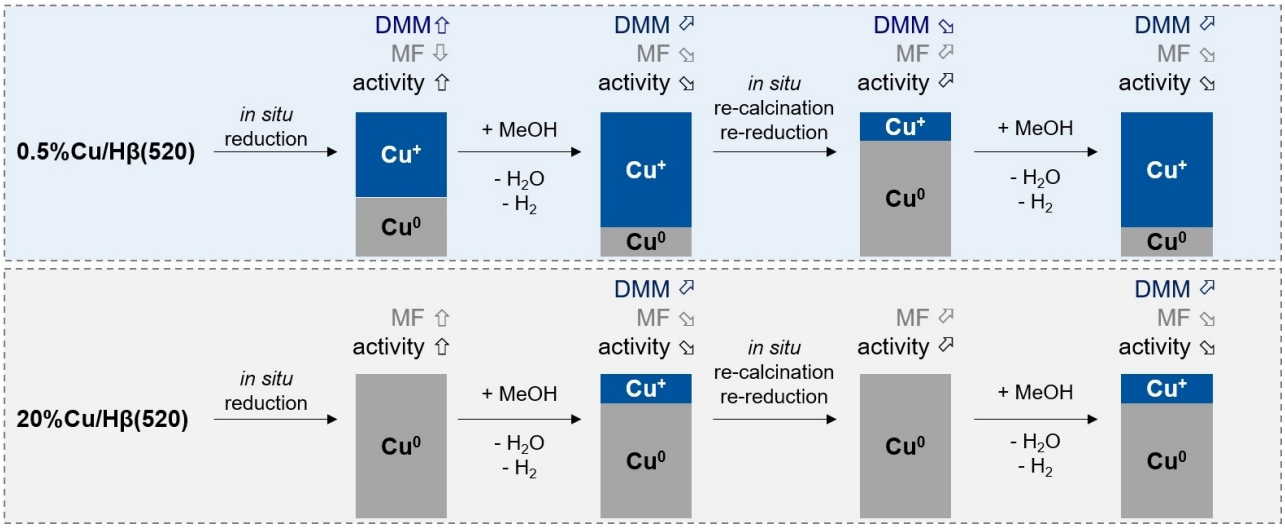

Figure 4. Proposed dynamics of Cu oxidation state of 0.5%Cu/Hβ(520) and 20%Cu/Hβ(520) and main products formed due to pre-treatment and reaction conditions. Herein, the Cu oxidation state dynamics is used as a descriptor since both the dehydrogenative and acidic functionality are affected by its change.

530 min TOS, which then decreases for the benefits of increasing DMM production, which reaches 16.0% selectivity after 1500 min TOS. This is accompanied by a rapid deactivation (*i.e.*, methanol conversion loss from 45.7%→15.1%). This might be explained by the gradual oxidation of Cu^0 species to Cu^+, possibly due to water which is formed during the initial production of DME, resulting in the increased formation of DMM at the expense of MF formation (Figure 4). Cu-based catalysts are known in literature for highly dynamic Cu oxidation states, which in turn depend on the substrates and products formed during a reaction, *e.g.* in the conversion of CO with NO or N_2O over Cu, Cu_2O, and CuO catalysts,[90] the photocatalytic H_2 evolution over various Cu species supported on Ti-based oxides,[91] or the electrochemical CO_2 reduction to ethylene over Cu-based electrodes.[92] *In situ* regeneration of 20%Cu/Hβ(520) restores the catalytic performance from the beginning of the initial reaction (*i.e.*, high methanol conversion and MF as main product), suggesting reversibility of the catalytic deactivation process and the dynamic reaction behavior. This underlines the hypothesis that the Cu oxidation state plays a crucial role in shaping both the product selectivity and activity of the catalyst, since it can be assumed that the Cu^+ species are reduced to Cu^0 species during the regeneration of the spent 20%Cu/Hβ(520) catalyst. However, to further verify how the catalytic activity and selectivity in the NOD of methanol depend on the Cu oxidation state, *in situ* or *in operando* XAFS and/or XPS studies would be required.

Figure S12, SI shows that the reaction reaches a steady state after 6000 min TOS with a selectivity towards MF and DMM of 48.3% and 42.6%, respectively, and a methanol conversion of 8.2%. This is especially interesting for a possible industrial application, because although MF and DMM have to be separated, the overall exergy efficiency of the dehydrogenative process is improved due to the intrinsic low H_2 consumption of the non-oxidative pathway compared to established oxidative routes for DMM production.[9,62]

Conclusions

In summary, we present that the product spectrum in the continuous gas-phase non-oxidative conversion of methanol can be shaped towards either of the valuable products DME, MF, and DMM with over 75% selectivity under the same reaction conditions (240 °C, 1 atm, 14549 mL/h/g_{cat}). This is possible by tailoring the bifunctional Cu/Hβ catalyst system according to its acidic and dehydrogenative properties by varying the SiO_2/Al_2O_3 ratio of the Hβ zeolite and the Cu loading, respectively. Very high DME selectivity (>99%) and methanol conversion (82.2%), as well as high stability of the catalyst are observed after 1500 min TOS when using 0.5%Cu/Hβ(25) as catalyst. When the SiO_2/Al_2O_3 ratio is increased to 520 *via* dealumination, DMM becomes the main product with a selectivity of 77.3% and a methanol conversion of 2.2% after 1500 min TOS. Next, the main product can be switched towards MF with a selectivity of 74.5% and a methanol conversion of 15.1% after 1500 min TOS, when the Cu loading on Hβ(520) is increased to 20 wt%. Together with characterizations such as XRD, H_2-TPR, CO-DRIFTS and py-FTIR, possible structure-activity relationships are proposed. A high concentration of acidic sites (both Brønsted and Lewis type) of 0.5%Cu/Hβ(25) is responsible for high DME formation from methanol condensation. When the SiO_2/Al_2O_3 ratio of the Hβ zeolite is increased to 520 by dealumination, only a low Lewis acidic site concentration is maintained and the acidic sites do not play a dominant role anymore in shaping the product selectivity, since DME formation is significantly diminished. Instead, the dehydrogenative properties, linked to the Cu oxidation state, shape the product selectivity towards either MF or DMM over the Cu/Hβ(520) catalysts. The presence of Cu^+ species on 0.5%Cu/Hβ(520) seems to be crucial for high DMM formation and the long induction time of >1500 min suggests a dynamic evolution of an appropriate Cu^+/Cu^0 ratio, which is in line with our previous results.[63] In contrast, solely Cu^0 species facilitate the formation of MF over 20%Cu/Hβ(520) *via* methanol dehydrogenation, which is in line with literature.[39,41,86,87] Deactivation of both 0.5%Cu/Hβ(520) and 20%Cu/Hβ(520) is linked to changes of the Cu oxidation state, which could successfully be restored after regeneration by an *in situ* re-calcination and re-reduction procedure.

Finally, we believe this study provides insights into the highly dynamic reaction network of the non-oxidative methanol conversion over the bifunctional Cu/Hβ catalyst system and suggests possible structure-activity relationships. This will in turn help to facilitate the rational design of catalysts for the conversion of methanol which is derived from sustainable feedstocks such as CO_2 and H_2 into environmentally friendly fuels and valuable chemicals such as DME, MF and DMM.

Experimental Section

Catalyst Preparation

Commercial NH_4β zeolite (SiO_2/Al_2O_3 = 25, abcr) was first calcined (550 °C, 10 °C/min, 5 h) in order to obtain Hβ zeolite. Hβ was then dealuminated according to an optimized procedure published earlier[63] by stirring 3 g of zeolite in 165 mL of 8 M HNO_3 (65%, CHEMSOLUTE®) at 80 °C and 500 rpm (under reflux) for 16 h. The dealuminated Hβ was then washed with 4 L of deionized water (until pH neutrality) and dried overnight at 110 °C. The Hβ supports are referred to as Hβ(25) and Hβ(520), respectively, where the number in brackets denotes the SiO_2/Al_2O_3 ratio of the zeolites as determined by ICP-OES in our previous work.[63] The introduction of Cu on the Hβ zeolite supports was performed *via* incipient wetness impregnation. For this, the appropriate amount of $Cu(NO_3)_2 \cdot 3\ H_2O$ (99%, ACROS ORGANICS) was dissolved in 0.5 mL of deionized water and added dropwise to 0.4 g of the respective Hβ support and the resulting mixture was stirred manually. The sample was then dried at 80 °C overnight, followed by calcination (450 °C with 5 °C/min for 3 h). The final catalysts are denoted as *X*%Cu/Hβ(*Y*), where *X* is the Cu loading in wt%, and *Y* is the SiO_2/Al_2O_3 ratio of the zeolite.

Catalyst Characterization

XRD measurements were performed on a D2 PHASER XE–T table-top X-ray analyzer from Bruker. The powder samples were measured in the 2θ range of 6–90 ° using Cu Kα radiation.

The Cu loading of the Cu/Hβ samples was determined by ICP-OES and analyses were carried out at Kolbe micro labs.

The nitrogen adsorption and desorption isotherms of the calcined Cu/Hβ catalysts were measured using a Quadrasorb SI unit from 3P Instruments at -196 °C. Prior to the measurement, the samples were degassed for 6 h in a FloVac degasser at 150 °C. The data was evaluated by means of the QuadraWin software. The specific surface area S_{BET} was determined according to the Brunauer–Emmett–Teller (BET) method in the p/p_0 range of 0.05–0.2. The micropore volume was quantified based on the t-plot model in the p/p_0 range of 0.2–0.4. The total pore volume was evaluated from the adsorbed N_2 volume at a p/p_0 ratio of 0.95.

For the H_2-TPR measurements, a ChemBet Pulsar TPR/TPD/TPO unit from Quantachrome Instruments which is equipped with a thermal conductivity detector (TCD) was employed. In a typical measurement, 100 mg of catalyst were first treated under He flow (22.4 mL/min) for 1 h at 150 °C to dry the sample, followed by a reduction in a 5 % H_2/Ar flow (18.6 mL/min) in a temperature range of 50–600 °C (5 °C/min).

CO-DRIFTS measurements were conducted on a Vertex 70 FT-IR spectrometer with a commercial high-temperature vacuum diffuse reflectance chamber as a sample cell equipped with ZnSe windows. Prior to CO adsorption, the powder samples were reduced *in situ* with a H_2-flow of 20 mL/min at 450 °C (20 °C/min) for 3 h. Then, the temperature was decreased to 30 °C under H_2 flow, and after reaching 30 °C, the flow was switched to N_2 and a background spectrum was collected. Subsequently, the sample was flushed with a gas mixture of 5 %CO/5 %He/N_2 to adsorb CO for 10 min until saturation. The sample was then purged with N_2 (20 mL/min) for 1 h and spectra were collected every 15 min to monitor the removal of weakly adsorbed CO from the sample.

Py-FTIR analysis was performed to investigate the Lewis and Brønsted acidic sites of the calcined Cu/Hβ catalysts, employing the same spectrometer which was used for CO-DRIFTS with a self-made stainless-steel transmission IR cell equipped with KBr windows. Thin self-supporting sample wafers were pressed, for which 100 mg KBr pellets were prepared with 15 mg catalyst of the samples with 0.5 wt% Cu loading, and 2.5 mg catalyst was used of the sample with 20 wt% Cu loading, since the 20 %Cu/Hβ(520) sample was absorbing IR radiation and needed to be diluted. In a typical measurement, the sample wafer was mounted to the transmission cell, followed by degassing at 250 °C (5 °C/min) for 1 h under vacuum (0.004 mbar). Then, the cell was cooled down to 80 °C and a background spectrum of the degassed sample prior to pyridine adsorption was recorded in a range of 8000–850 cm^{-1} with an optical resolution of 2 cm^{-1}. To investigate pyridine adsorption on the sample, first, pyridine vapor (~4.2 mbar) was introduced to the sample cell for 2 min at 80 °C and equilibrated for 30 min. Then, weakly adsorbed pyridine was desorbed from the sample at 200 °C (5 °C/min) under vacuum (0.004 mbar) for 30 min. Next, the cell was cooled down to 80 °C and a spectrum was collected. Subtracting the background spectrum (degassed sample prior to pyridine adsorption) gives the final pyridine spectrum.

Catalytic Tests

The gas-phase NOD of methanol was performed in a continuous flow fixed-bed reactor setup as described in our previous work.[62,63] Typically, 100 mg of catalyst was diluted with 0.9 g of SiC (200–450 mesh size) and loaded in the stainless steel tubular reactor. The catalyst was first reduced *in situ* at 450 °C with a H_2 flow of 20 mL/min for 3 h and then cooled down to room temperature under H_2 flow (10 mL/min). The reaction was performed at 240 °C and under previously optimized reaction conditions (1 atm, GHSV = 14549 mL/h*g_{cat}, $n(CH_3OH)/n(N_2) = 0.24$ (V/V)).[62,63] For this, methanol (99.8 %, CHEMSOLUTE®) with a flow of 0.008 mL/min and N_2 (19.4 mL/min) were pre-mixed in an evaporation chamber prior to the reactor inlet and introduced to the catalytic bed (the flow was stabilized for 1 h). All gas lines (inlet and outlet lines) and the evaporation chamber were heated to 140 °C to keep methanol and the products in the gas phase. The reaction products (DMM, MF, DME, CH_4, FA) and methanol were quantified using an online GC (Scion 456, Bruker, equipped with FID) which is connected to the reactor outlet. The gaseous products were also collected in gas bags and CO and CO_2 were quantified *via* an offline GC (Agilent HP 6890) and potential $C_{\geq 2}$ hydrocarbons were analyzed *via* another offline GC (Agilent 7890B). The selectivity to the respective products as well as methanol conversion are calculated based on the following equations.

$$S_P = \frac{N_P}{\sum N_i} \cdot 100\,\%$$

$$X = \left[1 - \left(\frac{N_{CH_3OH}}{\sum N_i}\right)\right] \cdot 100\,\%$$

Here, S_P denotes the selectivity towards the respective product P = DME, MF, or DMM. N_P is the concentration of carbon in either of the products P = DME, MF or DMM; N_i is the carbon concentration of all compounds in the outlet stream, X denotes methanol conversion, and N_{CH3OH} is the concentration of carbon in methanol. Typically, the catalytic performance comparison is based on the selectivity and methanol conversion after 1500 min TOS.

Acknowledgements

We acknowledge the research funding by DFG (PA 1689/22-1, Project ID: 512546329). N. S. thanks the German Federal Environmental Foundation for financial support. We would like to thank Frederico Boekhoff and Jannik Binding for their support with the laboratory work and Fabian Müller for his help with offline GC measurements for hydrocarbon quantification. We thank Noah Avraham-Radermacher for XRD analysis, and Hannelore Eschmann, Carina Frantzen, Heike Fickers-Boltz, Sandra Brosinski and Björn Johnen for offline GC analysis for CO and CO_2 quantification. Open Access funding enabled and organized by Projekt DEAL.

Conflict of Interests

The authors declare no conflict of interest.

Data Availability Statement

The data that support the findings of this study are available in the supplementary material of this article and on Zenodo under doi: 10.5281/zenodo.10938332.

Keywords: bifunctional Cu/Hβ catalyst · dimethoxymethane · dimethyl ether · methyl formate · non-oxidative methanol conversion

[1] H. Lee, K. Calvin, D. Dasgupta, G. Krinner, A. Mukherji, P. W. Thorne, C. Trisos, J. Romero, P. Aldunce, K. Barrett et al., *IPCC, 2023: Climate Change 2023: Synthesis Report. Contribution of Working Groups I, II and III to the Sixth Assessment Report of the Intergovernmental Panel on Climate Change [Core Writing Team, H. Lee and J. Romero (eds.)]. IPCC, Geneva, Switzerland*, Intergovernmental Panel on Climate Change (IPCC), **2023**.
[2] a) K. Räuchle, L. Plass, H.-J. Wernicke, M. Bertau, *Energy Technol.* **2016**, *4*, 193; b) M. Bertau, H. Offermanns, L. Plass, F. Schmidt, H.-J. Wernicke (Eds.) *Methanol: The Basic Chemical and Energy Feedstock of the Future. Asinger's Vision Today*, Springer, Berlin, Heidelberg, **2014**; c) M. Sterner, M. Specht, *Energies* **2021**, *14*, 6594; d) M. J. Palys, P. Daoutidis, *Comput. Chem. Eng.* **2022**, *165*, 107948.
[3] M. Bertau, K. Räuchle, H. Offermanns, *Chem. Unserer Zeit* **2015**, *49*, 312.
[4] M. Pan, W. Qian, R. Huang, X. Zhou, H. Huang, X. Pan, Z. Ban, *Energy Fuels* **2019**, *33*, 8683.
[5] N. M. Ribeiro, A. C. Pinto, C. M. Quintella, G. O. da Rocha, L. S. G. Teixeira, L. L. N. Guarieiro, M. do Carmo Rangel, M. C. C. Veloso, M. J. C. Rezende, R. Serpa da Cruz, et al., *Energy Fuels* **2007**, *21*, 2433.
[6] R. Sun, I. Delidovich, R. Palkovits, *ACS Catal.* **2019**, *9*, 1298.
[7] M. Härtl, P. Seidenspinner, E. Jacob, G. Wachtmeister, *Fuel* **2015**, *153*, 328.
[8] a) M. Härtl, P. Seidenspinner, G. Wachtmeister, E. Jacob, *MTZ Worldw* **2014**, *75*, 48; b) S. Hänggi, P. Elbert, T. Bütler, U. Cabalzar, S. Teske, C. Bach, C. Onder, *Energy Reports* **2019**, *5*, 555; c) S. Schemme, J. L. Breuer, M. Köller, S. Meschede, F. Walman, R. C. Samsun, P. Ralf, D. Stolten, *Int. J. Hydrogen Energy* **2020**, *8*, 5395.
[9] J. Burre, D. Bongartz, S. Deutz, C. Mebrahtu, O. Osterthun, R. Sun, S. Völker, A. Bardow, J. Klankermayer, R. Palkovits, et al., *Energy Environ. Sci.* **2021**, *14*, 3686.
[10] P. Styring, G. R. M. Dowson, I. O. Tozer, *Front. Energy Res.* **2021**, *9*.
[11] U. Mondal, G. D. Yadav, *J. CO2 Util.* **2019**, *32*, 299.
[12] W. Willems, M. Pannwitz, M. Zubel, J. Weber, *MTZ Worldw* **2020**, *81*, 26.
[13] E. G. Galanova, M. V. Magomedova, M. I. Afokin, A. V. Starozhitskaya, A. L. Maximov, *Catal. Commun.* **2021**, *153*, 106297.
[14] N. Mota, E. Millán Ordoñez, B. Pawelec, J. L. G. Fierro, R. M. Navarro, *Catalysts* **2021**, *11*, 411.
[15] J. Sun, G. Yang, Y. Yoneyama, N. Tsubaki, *ACS Catal.* **2014**, *4*, 3346.
[16] H. Bateni, C. Able, *Catal. Ind.* **2019**, *11*, 7.
[17] J. J. Spivey, *Chem. Eng. Commun.* **1991**, *110*, 123.
[18] Z. Azizi, M. Rezaeimanesh, T. Tohidian, M. R. Rahimpour, *Chem. Eng. Process.* **2014**, *82*, 150.
[19] a) K. C. Tokay, T. Dogu, G. Dogu, *Chem. Eng. J.* **2012**, *184*, 278; b) E.-Y. Lee, Y.-K. Park, O.-S. Joo, K.-D. Jung, *React. Kinet. Catal. Lett.* **2006**, *89*, 115.
[20] S. Sahebdelfar, P. M. Bijani, F. Yaripour, *Fuel* **2022**, *310*, 122443.
[21] a) A. E.-A. A. Said, M. N. Goda, M. A. Kassem, *Catal. Lett.* **2020**, *150*, 1714; b) Q. Sun, Y. Fu, H. Yang, A. Auroux, J. Shen, *J. Mol. Catal. A* **2007**, *275*, 183.
[22] D. Masih, S. Rohani, J. N. Kondo, T. Tatsumi, *Appl. Catal. B* **2017**, *217*, 247.
[23] O. O. Zhokh, A. I. Trypolskyi, *Theor. Exp. Chem.* **2021**, *57*, 220.
[24] V. Vishwanathan, K.-W. Jun, J.-W. Kim, H.-S. Roh, *Appl. Catal. A* **2004**, *276*, 251.
[25] Q. Tang, H. Xu, Y. Zheng, J. Wang, H. Li, J. Zhang, *Appl. Catal. A* **2012**, *413–414*, 36.
[26] G. Marsden, P. Kostetskyy, R.-S. Sekiya, A. Hoffman, S. Lee, R. Gounder, D. Hibbitts, L. J. Broadbelt, *ACS Materials Au* **2022**, *2*, 163.
[27] G. R. Moradi, F. Yaripour, P. Vale-Sheyda, *Fuel Process. Technol.* **2010**, *91*, 461.
[28] A. Gharibi Kharaji, M. Beheshti, S. Tangestani-nejad, O. Görke, H. R. Godini, *Asia-Pacific J. Chem. Eng.* **2020**, *15*.
[29] V. Barbarossa, R. Viscardi, A. Di Nardo, A. Santagata, *J. Chem. Technol. Biotechnol.* **2020**, *95*, 1739.
[30] a) C. Peinado, D. Liuzzi, R. M. Ladera-Gallardo, M. Retuerto, M. Ojeda, M. A. Peña, S. Rojas, *Sci. Rep.* **2020**, *10*, 8551; b) W. Alharbi, E. F. Kozhevnikova, I. V. Kozhevnikov, *ACS Catal.* **2015**, *5*, 7186.
[31] J. Sobczak, I. Wysocka, S. Murgrabia, A. Rogala, *Energies* **2022**, *15*, 5420.
[32] a) J. S. Lee, J. C. Kim, Y. G. Kim, *Appl. Catal.* **1990**, *57*, 1; b) G. Jenner, *Appl. Catal. A* **1995**, *121*, 25.
[33] L. Rong, Z. Xu, J. Sun, G. Guo, *J. Energy Chem.* **2018**, *27*, 238.
[34] D. Kaiser, L. Beckmann, J. Walter, M. Bertau, *Catalysts* **2021**, *11*, 869.
[35] T. Maier, M. Härtl, E. Jacob, G. Wachtmeister, *Fuel* **2019**, *256*, 115925.
[36] R. Sang, Z. Wei, Y. Hu, E. Alberico, D. Wei, X. Tian, P. Ryabchuk, A. Spannenberg, R. Razzaq, R. Jackstell, et al., *Nat. Catal.* **2023**, *6*, 543.
[37] a) D. Schneider, K.-D. Mohl, M. Schäfer, J. Paschold, J. H. Teles, S. Rittinge, US8957244B2, **2015**; b) E. Gérard, H. Götz, S. Pellegrini, Y. Castanet, A. Mortreux, *Appl. Catal. A* **1998**, *170*, 297.
[38] a) M. Yoneoka, M. Osugi, US4149009 A, **1979**; b) X. Huang, N. W. Cant, M. S. Wainwright, L. Ma, *Chem. Eng. Process.* **2005**, *44*, 393.
[39] D.-J. Yuan, A. M. Hengne, Y. Saih, K.-W. Huang, *ACS Omega* **2019**, *4*, 1854.
[40] Z. Lu, D. Gao, H. Yin, A. Wang, S. Liu, *J. Ind. Eng. Chem.* **2015**, *31*, 301.
[41] H. Yang, Y. Chen, X. Cui, G. Wang, Y. Cen, T. Deng, W. Yan, J. Gao, S. Zhu, U. Olsbye et al, *Angew. Chem. Int. Ed.* **2018**, *57*, 1836.
[42] A. Guerrero-Ruiz, I. Rodriguez-Ramos, J. Fierro, *Appl. Catal.* **1991**, *72*, 119.
[43] T. P. Minyukova, I. I. Simentsova, A. V. Khasin, N. V. Shtertser, N. A. Baronskaya, A. A. Khassin, T. M. Yurieva, *Appl. Catal. A* **2002**, *237*, 171.
[44] a) Z. Li, J. Xu, X. Gu, K. Wang, W. Wang, X. Zhang, Z. Zhang, Y. Ding, *ChemCatChem* **2013**, *5*, 1705; b) D.-H. Wang, K. M. Engle, B.-F. Shi, J.-Q. Yu, *Science* **2010**, *327*, 315.
[45] B. Indu, W. R. Ernst, L. T. Gelbaum, *Ind. Eng. Chem. Res.* **1993**, *32*, 981.
[46] K. M. K. Yu, C. M. Y. Yeung, S. C. Tsang, *J. Am. Chem. Soc.* **2007**, *129*, 6360.
[47] a) K. Czelej, K. Cwieka, J. C. Colmenares, K. J. Kurzydlowski, Y.-J. Xu, *ACS Appl. Mater. Interfaces* **2017**, *9*, 31825; b) C. Li, X. Yang, G. Gao, Y. Li, W. Zhang, X. Chen, H. Su, S. Wang, Z. Wang, *Catal. Sci. Technol.* **2019**, *9*, 6240.
[48] R. Kishi, H. Ogihara, M. Yoshida-Hirahara, K. Shibanuma, I. Yamanaka, H. Kurokawa, *ACS Sustainable Chem. Eng.* **2020**, *8*, 11532.
[49] N. Westhues, M. Belleflamme, J. Klankermayer, *ChemCatChem* **2019**, *11*, 5269.
[50] R. Sun, A. Kann, H. Hartmann, A. Besmehn, P. J. C. Hausoul, R. Palkovits, *ChemSusChem* **2019**, *12*, 3278.
[51] a) C. H. Gierlich, K. Beydoun, J. Klankermayer, R. Palkovits, *Chem. Ing. Tech.* **2020**, *92*, 116; b) A. Omari, B. Heuser, S. Pischinger, *Fuel* **2017**, *209*, 232; c) H. Liu, Z. Wang, J. Wang, X. He, Y. Zheng, Q. Tang, J. Wang, *Energy* **2015**, *88*, 793; d) J. Burre, D. Bongartz, A. Mitsos, *Ind. Eng. Chem. Res.* **2019**, *58*, 5567; e) A. Omari, B. Heuser, S. Pischinger, C. Rüdinger, *Appl. Energy* **2019**, *239*, 1242.
[52] J. Burger, M. Siegert, E. Ströfer, H. Hasse, *Fuel* **2010**, *89*, 3315.
[53] S. Deutz, D. Bongartz, B. Heuser, A. Kätelhön, L. Schulze Langenhorst, A. Omari, M. Walters, J. Klankermayer, W. Leitner, A. Mitsos, et al., *Energy Environ. Sci.* **2018**, *11*, 331.
[54] L. Lautenschütz, D. Oestreich, P. Seidenspinner, U. Arnold, E. Dinjus, J. Sauer, *Fuel* **2016**, *173*, 129.
[55] D. Bongartz, J. Burre, A. Mitsos, *Ind. Eng. Chem. Res.* **2019**, *58*, 4881.
[56] a) C. J. Baranowski, A. M. Bahmanpour, O. Kröcher, *Appl. Catal. B* **2017**, *217*, 407; b) A. Fink, C. H. Gierlich, I. Delidovich, R. Palkovits, *ChemCatChem* **2020**, *12*, 5710.
[57] J. Wang, Y. Zheng, S. Wang, T. Wang, S. Chen, C. Zhu, U. S. Patent No. 9,266,990, **2016**.
[58] K. Thavornprasert, M. Capron, L. Jalowiecki-Duhamel, F. Dumeignil, *Catal. Sci. Technol.* **2016**, *6*, 958.
[59] Y. L. Bai, X. Dai, T. L. Cao, W. Qi, *ChemCatChem* **2023**.
[60] a) A. W. Franz, H. Kronemayer, D. Pfeiffer, R. D. Pilz, G. Reuss, W. Disteldorf, A. O. Gamer, A. Hilt in *Ullmann's Encyclopedia of Industrial Chemistry*, Wiley-VCH Verlag GmbH & Co. KGaA, **2016**, pp. 1–34; b) D. Bongartz, L. Doré, K. Eichler, T. Grube, B. Heuser, L. E. Hombach, M. Robinius, S. Pischinger, D. Stolten, G. Walther et al, *Appl. Energy* **2018**, *231*, 757; c) M. Held, Y. Tönges, D. Pélerin, M. Härtl, G. Wachtmeister, J. Burger, *Energy Environ. Sci.* **2019**, *12*, 1019.
[61] a) K. Thenert, K. Beydoun, J. Wiesenthal, W. Leitner, J. Klankermayer, *Angew. Chem. Int. Ed.* **2016**, *55*, 12266; b) B. G. Schieweck, J. Klankermayer, *Angew. Chem. Int. Ed.* **2017**, *56*, 10854.

[62] R. Sun, C. Mebrahtu, J. P. Hofmann, D. Bongartz, J. Burre, C. H. Gierlich, P. J. C. Hausoul, A. Mitsos, R. Palkovits, *Sustain. Energy Fuels* **2021**, *5*, 117.
[63] C. Mebrahtu, R. Sun, C. Gierlich, R. Palkovits, *Appl. Catal. B* **2021**, *287*, 119964.
[64] A. T. To, T. J. Wilke, E. Nelson, C. P. Nash, A. Bartling, E. C. Wegener, K. A. Unocic, S. E. Habas, T. D. Foust, D. A. Ruddy, *ACS Sustainable Chem. Eng.* **2020**, *8*, 12151.
[65] J. Ren, Y. Xu, C. Ye, M. Peng, F. Xin, *Chem. Eng. J.* **2024**, *479*, 147774.
[66] M. Thommes, K. Kaneko, A. V. Neimark, J. P. Olivier, F. Rodriguez-Reinoso, J. Rouquerol, K. S. Sing, *Pure Appl. Chem.* **2015**, *87*, 1051.
[67] C. J. Baranowski, M. Roger, A. M. Bahmanpour, O. Kröcher, *ChemSusChem* **2019**, *12*, 4421.
[68] K. Momma, F. Izumi, *J. Appl. Crystallogr.* **2011**, *44*, 1272.
[69] H. Wang, R. Xu, Y. Jin, R. Zhang, *Catal. Today* **2019**, *327*, 295.
[70] L. Xu, C. Shi, Z. Zhang, H. Gies, F.-S. Xiao, D. de Vos, T. Yokoi, X. Bao, M. Feyen, S. Maurer, et al., *Microporous Mesoporous Mater.* **2014**, *200*, 304.
[71] R. Bulánek, B. Wichterlová, Z. Sobalík, J. Tichý, *Appl. Catal. B* **2001**, *31*, 13.
[72] J. Y. Yan, G.-D. Lei, W. Sachtler, H. H. Kung, *J. Catal.* **1996**, *161*, 43.
[73] a) G. T. Palomino, S. Bordiga, A. Zecchina, G. L. Marra, C. Lamberti, *J. Phys. Chem. B* **2000**, *104*, 8641; b) J. Xue, X. Wang, G. Qi, J. Wang, M. Shen, W. Li, *J. Catal.* **2013**, *297*, 56; c) J. Hun Kwak, H. Zhu, J. H. Lee, C. H. F. Peden, J. Szanyi, *Chem. Commun. (Camb.)* **2012**, *48*, 4758; d) V. Y. Borovkov, M. Jiang, Y. Fu, *J. Phys. Chem. B* **1999**, *103*, 5010; e) S. Kannan, T. Venkov, K. Hadjiivanov, H. Knözinger, *Langmuir* **2004**, *20*, 730.
[74] L. Wang, W. Li, G. Qi, D. Weng, *J. Catal.* **2012**, *289*, 21.
[75] J. Engeldinger, C. Domke, M. Richter, U. Bentrup, *Appl. Catal. A* **2010**, *382*, 303.
[76] D. Yu, W. Dai, G. Wu, N. Guan, L. Li, *Chin. J. Catal.* **2019**, *40*, 1375.
[77] a) T. D. Conesa, J. M. Hidalgo, R. Luque, J. M. Campelo, A. A. Romero, *Appl. Catal. A* **2006**, *299*, 224; b) L. Li, C. Stroobants, K. Lin, P. A. Jacobs, B. F. Sels, P. P. Pescarmona, *Green Chem.* **2011**, *13*, 1175; c) S. B. Kim, S. J. You, Y. T. Kim, S. Lee, H. Lee, K. Park, E. D. Park, *Korean J. Chem. Eng.* **2011**, *28*, 710; d) M. Tamura, K. Shimizu, A. Satsuma, *Appl. Catal. A* **2012**, *433–434*, 135.
[78] J. Weitkamp, *Solid State Ionics* **2000**, *131*, 175.
[79] M. H. W. Sonnemans, C. den Heijer, M. Crocker, *J. Phys. Chem.* **1993**, *97*, 440.
[80] a) A. Sultana, T. Nanba, M. Haneda, M. Sasaki, H. Hamada, *Appl. Catal. B* **2010**, *101*, 61; b) P. Manjunathan, S. P. Maradur, A. B. Halgeri, G. V. Shanbhag, *J. Mol. Catal. A* **2015**, *396*, 47.
[81] a) D. M. Sung, Y. H. Kim, E. D. Park, J. E. Yie, *Res. Chem. Intermed.* **2010**, *36*, 653; b) A. R. Keshavarz, M. Rezaei, F. Yaripour, *Powder Technol.* **2010**, *199*, 176.
[82] M. A. Armenta, R. Valdez, J. M. Quintana, R. Silva-Rodrigo, L. Cota, A. Olivas, *Int. J. Hydrogen Energy* **2018**, *43*, 6551.
[83] E. Catizzone, A. Aloise, E. Giglio, G. Ferrarelli, M. Bianco, M. Migliori, G. Giordano, *Catal. Commun.* **2021**, *149*, 106214.
[84] N. Shimoda, K. Faungnawakij, R. Kikuchi, K. Eguchi, *Appl. Catal. A* **2010**, *378*, 234.
[85] a) A. Prašnikar, A. Pavlišič, F. Ruiz-Zepeda, J. Kovač, B. Likozar, *Ind. Eng. Chem. Res.* **2019**, *58*, 13021; b) A. J. Martín, S. Mitchell, C. Mondelli, S. Jaydev, J. Pérez-Ramírez, *Nat. Catal.* **2022**, *5*, 854.
[86] N. Wang, Y. Quan, J. Zhao, H. Li, J. Ren, *Molecular Catalysis* **2021**, *505*, 111514.
[87] Y. Jin, Y. Quan, Y. Li, J. Zhao, J. Ren, *Fuel* **2024**, *355*, 129546.
[88] R. Kefirov, A. Penkova, K. Hadjiivanov, S. Dzwigaj, M. Che, *Microporous Mesoporous Mater.* **2008**, *116*, 180.
[89] L. Wu, B. Li, C. Zhao, *ChemCatChem* **2018**, *10*, 1140.
[90] H. Iwamoto, S. Kameoka, Y. Xu, C. Nishimura, A. P. Tsai, *J. Phys. Chem. Solids* **2019**, *125*, 64.
[91] V. Polliotto, S. Livraghi, A. Krukowska, M. V. Dozzi, A. Zaleska-Medynska, E. Selli, E. Giamello, *ACS Appl. Mater. Interfaces* **2018**, *10*, 27745.
[92] T.-C. Chou, C.-C. Chang, H.-L. Yu, W.-Y. Yu, C.-L. Dong, J.-J. Velasco-Vélez, C.-H. Chuang, L.-C. Chen, J.-F. Lee, J.-M. Chen, et al., *J. Am. Chem. Soc.* **2020**, *142*, 2857.

Manuscript received: December 21, 2023
Revised manuscript received: March 13, 2024
Accepted manuscript online: March 21, 2024
Version of record online: April 15, 2024